Independent activation of distinct pores in dimeric TMEM16A channels

Grace Jeng,[1] Muskaan Aggarwal,[1] Wei-Ping Yu,[1] and Tsung-Yu Chen[1,2]

[1]Center for Neuroscience and [2]Department of Neurology, University of California, Davis, Davis, CA 95618

The TMEM16 family encompasses Ca^{2+}-activated Cl^- channels (CaCCs) and lipid scramblases. These proteins are formed by two identical subunits, as confirmed by the recently solved crystal structure of a TMEM16 lipid scramblase. However, the high-resolution structure did not provide definitive information regarding the pore architecture of the TMEM16 channels. In this study, we express TMEM16A channels constituting two covalently linked subunits with different Ca^{2+} affinities. The dose–response curve of the heterodimer appears to be a weighted sum of two dose–response curves—one corresponding to the high-affinity subunit and the other to the low-affinity subunit. However, fluorescence resonance energy transfer experiments suggest that the covalently linked heterodimeric proteins fold and assemble as one molecule. Together these results suggest that activation of the two TMEM16A subunits likely activate independently of each other. The Ca^{2+} activation curve for the heterodimer at a low Ca^{2+} concentration range ($[Ca^{2+}] < 5$ µM) is similar to that of the wild-type channel—the Hill coefficients in both cases are significantly greater than one. This suggests that Ca^{2+} binding to one subunit of TMEM16A is sufficient to activate the channel and that each subunit contains more than one Ca^{2+}-binding site. We also take advantage of the I-V curve rectification that results from mutation of a pore residue to address the pore architecture of the channel. By introducing the pore mutation and the mutation that alters Ca^{2+} affinity in the same or different subunits, we demonstrate that activation of different subunits appears to be associated with the opening of different pores. These results suggest that the TMEM16A CaCC may also adopt a "double-barrel" pore architecture, similar to that found in CLC channels and transporters.

INTRODUCTION

Members of the TMEM16 gene family are transmembrane proteins classified into two functional categories: Ca^{2+}-activated ion channels (Caputo et al., 2008; Schroeder et al., 2008; Yang et al., 2008) and phospholipid scramblases (Suzuki et al., 2010, 2013; Yang et al., 2012; Malvezzi et al., 2013). TMEM16A and TMEM16B in this family form Ca^{2+}-activated Cl^- channels (CaCCs) critical for various physiological processes, including regulation of smooth muscle contraction, transepithelial fluid secretion, and neuronal excitation, etc. (Hartzell et al., 2005; Huang et al., 2012; Scudieri et al., 2012). In contrast, TMEM16C through TMEM16J may function as lipid scramblases (Suzuki et al., 2013), the defect of which causes a variety of diseases, including gnathodiaphyseal dysplasia of bones (Katoh and Katoh, 2004; Tsutsumi et al., 2004; Marconi et al., 2013), muscular dystrophy (Bolduc et al., 2010; Mahjneh et al., 2010; Hicks et al., 2011), and a blood coagulation problem known as Scott syndrome (Suzuki et al., 2010; Lhermusier et al., 2011; Bevers and Williamson, 2016), to name a few. Activation of TMEM16A or TMEM16B generates mostly Cl^--selective currents, whereas activation of TMEM16F induces ionic currents contributed by anions (Grubb et al., 2013; Shimizu et al., 2013), and possibly also by cations (Yang et al., 2012; Adomaviciene et al., 2013; Yu et al., 2015a). The functional dichotomy and different ion selectivity associated with these two types of TMEM16 members are intriguing research subjects (Kunzelmann et al., 2014; Pedemonte and Galietta, 2014; Picollo et al., 2015).

Biochemical evidence suggests that a functional TMEM16 molecule is composed of two subunits (Fallah et al., 2011; Sheridan et al., 2011; Tien et al., 2013). The recently solved crystal structure of a TMEM16 family member from the fungus *Nectria haematococca* (nhTMEM16) confirmed that TMEM16 molecules adopt a homodimeric architecture (Brunner et al., 2014), similar to that observed in members of the CLC Cl^- channel/transporter family (Dutzler et al., 2002, 2003). In addition, the high-resolution structure of nhTMEM16 (Fig. 1 A) revealed that each subunit of the TMEM16 molecule binds two Ca^{2+} ions via several chelating acidic residues (Brunner et al., 2014). Mutations of the corresponding acidic residues in TMEM16A greatly alter the apparent Ca^{2+} affinity in activating the channel: the half-activation concentration ($K_{1/2}$) of the wild-type TMEM16A channel is in the submicromolar to micromolar range, whereas those of the mutants can increase by two to three orders of magnitude! Thus, these acidic residues, including the first two identified glutamate residues, E698 and E701 (Yu et al., 2012),

Correspondence to Tsung-Yu Chen: tycchen@ucdavis.edu

Abbreviations used: CaCC, Ca^{2+}-activated Cl^- channel; FRET, fluorescence resonance energy transfer; RI, rectification index.

The Rockefeller University Press $30.00
J. Gen. Physiol. 2016 Vol. 148 No. 5 393–404
https://doi.org/10.1085/jgp.201611651

Supplemental material can be found at:
http://doi.org/10.1085/jgp.201611651

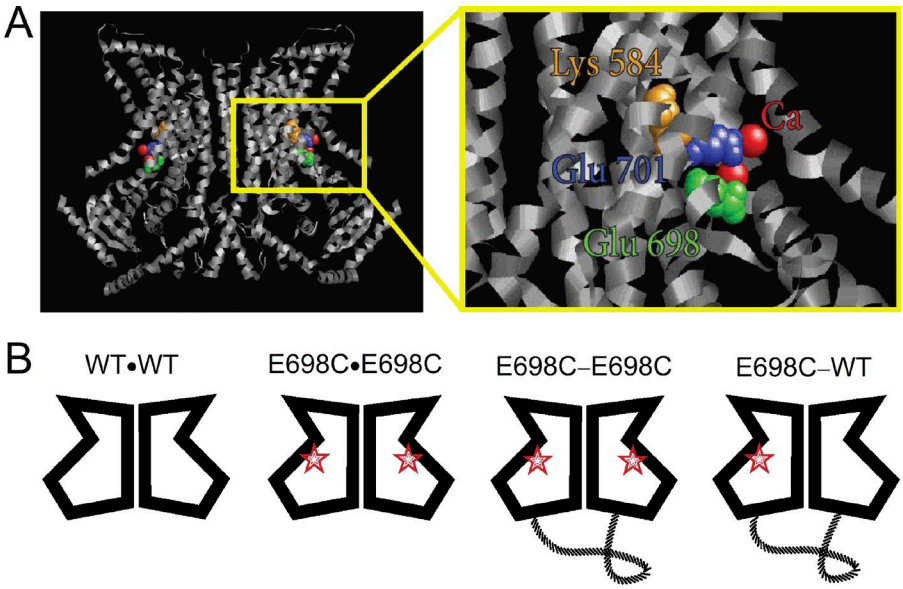

Figure 1. **Constructing a covalently linked tandem dimer of the TMEM16A channel.** (A) Structure of the nhTMEM16 molecule, showing the positions of corresponding amino acid residues, the mutations of which alter the Ca^{2+} affinity (E698 and E701) and current rectification (K584) of the TMEM16A channel. The nhTMEM16 residues corresponding to K584, E698, and E701 of TMEM16A are N378, E503, and E506, respectively. (B) Schematic diagrams and the nomenclature of various homodimeric and heterodimeric TMEM16A constructs. Red stars represent the E698C mutation.

along with the three additional acidic residues E650, E730, and D734 (Tien et al., 2014), participate in forming the Ca^{2+}-binding sites.

As TMEM16 proteins adopt a dimeric architecture similar to that of the CLC chloride channels/transporters, which are known to consist of two independent ion transport pathways, it is tempting to ask whether the TMEM16A channel also consists of two pores, and if so, whether the two pores function independently. These questions were unanswered because the nhTMEM16 structure did not provide definitive information for identifying the channel pore or pores. We constructed covalently linked tandem dimers of TMEM16A and introduced mutations that alter Ca^{2+} affinity to only one subunit. By doing so, we were able to create TMEM16A channels containing two subunits with different Ca^{2+}-binding affinities. Our results demonstrate that activation of the two subunits appears to be mostly independent, although cooperativity between activation of the two subunits cannot be ruled out. By introducing a pore mutation in only one subunit, we further demonstrate that the current generated by activating the different subunits may come through distinct pores.

MATERIALS AND METHODS

Molecular biology and channel expression

The wild-type mouse TMEM16A (mTMEM16A) cDNA (NCBI reference sequence: NM_001242349.1), which is the "*a*" alternative splice variant (Ferrera et al., 2009), was a courtesy from L.Y. Jan (University of California, San Francisco, San Francisco, CA). In comparison with the "*a, c*" splice variant used in the companion paper by Lim et al., the sequence referred in this paper is four residues shorter. For example, residues K584 and E698 referred in this paper correspond to K588 and E702, respectively, in Lim et al. (2016). The monomeric and tandem dimeric wild-type and mutant cDNA constructs were subcloned in pEGFP-N3 or pIRES2 expression vectors (Takara Bio Inc.). Mutagenesis was achieved by using the QuikChange II site-directed mutagenesis kit (Agilent Technologies). To make the TMEM16A tandem dimer, the cDNA of TMEM16A without stop codon was subcloned into the 5′ end of another TMEM16A cDNA already in the pIRES2 construct. The linker between the two subunits was thus encoded by the nucleotide sequence of the 5′ untranslated region of the second subunit, leading to an insertion of 33 amino acids of the following sequence linking two subunits: TGGPETIAHEAQDAGTPNSGDATGVVDGEREAT. For simplicity, the symbols WT and MT will be used to represent the wild-type and the affinity-altered mutant subunit, respectively. Furthermore, WT•WT represents the wild-type TMEM16A channel expressed from the monomeric cDNA construct, whereas the channel expressed from the monomeric E698C mutant cDNA will be called E698C•E698C (the two subunits naturally assemble together). The tandem dimeric channels generated from linking two WT subunits, one E698C and one WT subunit, and two E698C subunits will be called WT-WT, E698C-WT, and E698C-E698C, respectively (Fig. 1 B). The same principle of nomenclature is used for the E701C constructs. The K584Q mutant represents the channel in which both WT subunits contain the K584Q mutation. The symbols E698C(K584Q)-WT or E698C-WT(K584Q) will be used when the mutation K584Q is introduced specifically to the E698C or the WT subunit of the E698C-WT heterodimer.

The aforementioned cDNA constructs produced channels with a GFP attached to the C terminus of the channel proteins (in pEGFP-N3 construct) or channels without a GFP tag but with a separate GFP protein ex-

pressed in the same cell. The functional properties of the GFP-tagged and untagged TMEM16A were not distinguishable. Transfections of cDNAs to human embryonic kidney (HEK) 293 cells were performed using the Lipofectamine transfection method (Ni et al., 2014; Yu et al., 2014, 2015b). Cells expressing channels were identified by the green fluorescence in an inverted microscope (DM IRB; Leica) equipped with a fluorescent light source and a GFP filter (Chroma Technology Corp.).

Electrophysiological experiments

Excised inside-out patch recordings from GFP-positive HEK293 cells were conducted 24–72 h after transfections. The extracellular (pipette) solution contained 140 mM NaCl, 10 mM HEPES, and 0.1 mM EGTA and had a pH of 7.4; this solution was defined to be the 0-Ca^{2+} solution. The intracellular solutions contained various concentrations of EGTA ([EGTA]) and [Ca^{2+}], with free [Ca^{2+}] ranging from ∼0.1 µM to 20 mM (Ni et al., 2014; Yu et al., 2014). To construct [Ca^{2+}]-dependent activation curves, all intracellular solutions contained 10 mM HEPES and had a final [Cl^-] of 140 mM. [EGTA] of 0.1 mM was used for solutions with free [Ca^{2+}] between 5 µM and 20 mM. For solutions containing 2–20 mM [Ca^{2+}], the [NaCl] required for making final 140 mM [Cl^-] was reduced according to the required [$CaCl_2$]. For example, for the solution containing 20 mM [Ca^{2+}], 100 mM NaCl, and 20.1 mM $CaCl_2$ were added in the solution in addition to 0.1 mM EGTA. Solutions containing free [Ca^{2+}] < 5 µM required higher Ca^{2+}-buffered capacity, and thus 1 mM [EGTA] was used in these solutions. The required amounts of total Ca^{2+} for generating specific free [Ca^{2+}] were calculated using the MaxChelator program with constants from the NIST database #46 v8 available on the internet (http://maxchelator.stanford.edu/CaEGTA-NIST.htm). All values of [Ca^{2+}] referred in this paper are free [Ca^{2+}], whereas total [Ca^{2+}] added to the solutions are stated as [$CaCl_2$].

The working solutions for constructing current-voltage relationship (or I-V curve) were made from four stock solutions, 1× NaCl and 1× NMDG-SO_4 solutions, which contained 10 mM HEPES and 0.1 mM EGTA with or without 0.12 mM [$CaCl_2$], pH 7.4. The two 1× NaCl solutions contained 140 mM NaCl and thus were equivalent to the solutions with 0 and 20 µM [Ca^{2+}] used in the dose–response experiments (140 mM NaCl, 10 mM HEPES, and 0.1 mM EGTA, with or without 0.12 mM [$CaCl_2$], pH 7.4). The 1× NMDG-SO_4 solutions contained 140 mM NMDG buffered with sulfuric acid (H_2SO_4) to pH 7.4. Three working solutions, 1×, 0.6×, and 0.3× NaCl solutions, were made by mixing the 1× NaCl solution with the 1× NMDG-SO_4 solution in 1:0, 0.6:0.4, and 0.3:0.7 volume ratios, respectively, resulting in solutions containing 140 mM, 84 mM, and 42 mM [NaCl], respectively. In separate control experiments, $NMDG^+$ and SO_4^{2-} did not carry detectable current through the TMEM16A channel. The junction potential between 1× NaCl and 1× NMDG-SO_4 solutions calculated using the Clampfit program (Molecular Devices) was only ∼2 mV. The differences of junction potentials between any two of the three intracellular solutions were thus negligible (the largest junction potential was 1.6 mV between 1× and 0.3× NaCl solutions) and were not corrected in I-V curve experiments.

Recording electrodes were made from borosilicate glass capillaries (World Precision Instruments) using the PP830 electrode puller (Narishige). When filled with the extracellular pipette solution, the resistance of the electrodes was between ∼1.5 and ∼3.0 MΩ. All experiments were performed using the Axopatch 200B amplifier and the Digidata1440 analogue-digital signal-converting board controlled by the pClamp10 software (Molecular Devices). Various solutions were delivered to the intracellular side of the excised inside-out patch using the SF-77 solution exchanger (Warner Instruments). To construct dose–response curves, we used a three-pulse protocol described previously (Ni et al., 2014), in which the cytoplasmic side of the patch was sequentially exposed to saturating [Ca^{2+}] (20 µM for the wild-type channel and 20 mM for the channels containing E698C or E701C mutations), a test [Ca^{2+}], and then again the saturating [Ca^{2+}] (Fig. 2). In each recording trace, the current amplitude in 0-Ca^{2+} solution was subtracted from that obtained in the presence of Ca^{2+}. The current activated by the test [Ca^{2+}] was then normalized to the mean of the two maximum currents activated by the saturating [Ca^{2+}] (or the maximum [Ca^{2+}] in the case of E701C), and the normalized values were used for generating dose–response curves.

To construct I-V curves, two voltage protocols were used in various intracellular [NaCl] with or without 20 µM [Ca^{2+}] (Figs. 6 and 7). In one, a ramp voltage change (duration 1.6 s) from −80 to 80 mV was applied. The other voltage protocol used step voltage jumps from a holding voltage of 0 mV to a test voltage from −80 to 80 mV in a 20-mV step. Instantaneous current within 10 ms of voltage jump to the test voltage was measured. For each patch, the recordings in 0-Ca^{2+} solutions were subtracted from that obtained in [Ca^{2+}] (20 µM or 20 mM), and the resulting leak-subtracted I-V curves were used to determine the reversal potential (Fig. 6). To average I-V curves from different membrane patches, the digitized data points from the ramp protocol were normalized to the last digitized point obtained at 80 mV (Fig. 7, B and C). For the current obtained at different step voltages, the instantaneous currents measured at different voltages were normalized to that measured at 80 mV. These two voltage protocols gave nearly identical I-V curves as shown in Fig. 7 B.

Experimental data were analyzed using Clampfit 10.4 software (Molecular Devices) and Origin Pro 8.0 soft-

ware (OriginLab, Co.). All averaged data were presented as mean ± SEM. The dose–response results obtained in $[Ca^{2+}]$ up to 10 mM, after being normalized to the current obtained at 20 mM $[Ca^{2+}]$, were fitted to the Hill equation to evaluate the apparent Ca^{2+} affinity: $I_{norm} = 1/(1 + (K_{1/2}/[Ca^{2+}])^h)$, where I_{norm} is the normalized current and $K_{1/2}$ and h are the fitted half-effective concentration and the Hill coefficient, respectively.

To evaluate the permeability ratio P_{Cl}/P_{Na}, reversal potentials (E_{rev}) of the I-V curves were determined in the presence of various intracellular solutions containing 1× (140 mM), 0.6×, and 0.3× [NaCl], whereas the extracellular solution contained 1× [NaCl]. The relationship between E_{rev} and P_{Cl}/P_{Na} follows the Goldman-Hodgkin-Katz equation:

$$E_{rev} = \left(\frac{RT}{F}\right)\ln\left(\frac{P_{Na}[Na^+]_o + P_{Cl}[Cl^-]_i}{P_{Na}[Na^+]_i + P_{Cl}[Cl^-]_o}\right).$$

The degree of the I-V curve rectification was evaluated by a rectification index (RI), which is defined as the ratio of the absolute current amplitudes at −80 and 80 mV in symmetrical 140 mM $[Cl^-]$. Namely, $RI = -I_{-80\,mV}/I_{80\,mV}$. Thus, a linear I-V curve will have an RI close to 1 but RI < 1 for outwardly rectified I-V curves.

Fluorescence resonance energy transfer (FRET) experiments

FRET experiments were performed according to the previously described spectroFRET approach (Bykova et al., 2006; Yu et al., 2015b). In brief, the experiments were conducted with an inverted fluorescence microscope (IX-81; Olympus) equipped with a 100-W mercury lamp. The intensity and the duration of fluorescent light exposure were controlled by a computer-driven neutral density filter and a shutter, using MetaMorph software (Molecular Devices/Invitrogen). A CCD camera (Roper 128B) was used, and MetaMorph user-designed journals initiated automatic collection of fluorescence cell images and their spectral images obtained by feeding the cell images through a spectrograph (Acton SpectraPro 2150i). For obtaining the spectra of the FRET donor (cerulean, abbreviated as "C") and FRET acceptor (eYFP, abbreviated as "Y"), the excitation light wavelengths were controlled by two filter cubes (Chroma Technology Corp.) filtering the excitation light for C (cube I: excitation filter D436/20 and dichroic mirror 455dclp) and Y (cube II: excitation filter HQ500/20 and dichroic mirror Q515lp). No emission filter was used in these two filter cubes. Background light spectra from the blank region in the same image were subtracted from the spectra of the fluorophores.

Fluorescence analyses were conducted as described previously (Bykova et al., 2006; Yu et al., 2015b). Theoretically, the efficiency of the energy transfer (E) depends on the distance, R, between the two fluorophores according to the Förster equation, $E = (R_0)^6/[(R_0)^6 + R^6]$, where R_0 is a spectroscopically determined distance when E = 0.5 (or 50% of FRET efficiency). In practice, because the FRET donor–containing subunit and the FRET acceptor–containing subunit are coexpressed, the channel molecules can contain two FRET donors, two FRET acceptors, or one donor and one acceptor. For cells expressing many more acceptor-containing subunits but a very small number of donor-containing subunits, the apparent FRET efficiency (E_{app}) will be very small because of the presence of many molecules containing two FRET acceptors, whereas a cell with a high donor/acceptor ratio will give a value of E_{app} approaching the true FRET efficiency. Therefore, the FRET efficiency depends on the ratio of the expressed donor and acceptor molecules in the cells. We calculated the FRET efficiency from individual cells by the approach briefly described below (for more detailed description, see Bykova et al., 2006; Yu et al., 2015b). From cells expressing only the FRET acceptor (Y)–tagged subunit, ratio A_0 is determined as the ratio between the fluorescence excited by the light passing cube I ($F^{Y(Direct)}{}_{436}$) and the fluorescence excited by the cube II–filtered light ($F^{Y}{}_{500}$). Namely, ratio $A_0 = F^{Y(Direct)}{}_{436}/F^{Y}{}_{500}$. From cells cotransfected with donor (C)-containing subunits and acceptor (Y)-containing subunits, we determined another ratio, ratio A. In this case, the spectrum from cells expressing C only was first subtracted from the C excitation spectrum obtained from cells coexpressing C and Y, resulting in a Y-only spectrum, which includes two components: the Y emission caused by FRET ($F^{Y(FRET)}{}_{436}$) and the emission caused by direct excitation of Y ($F^{Y(Direct)}{}_{436}$). Thus, ratio $A = F^{Y}{}_{436}/F^{Y}{}_{500} = (F^{Y(FRET)}{}_{436} + F^{Y(Direct)}{}_{436})/F^{Y}{}_{500}$. The FRET ratio (FR) was defined as the ratio of A and A_0: FR = ratio A/ratio $A_0 = (F^{Y(FRET)}{}_{436} + F^{Y(Direct)}{}_{436})/F^{Y(Direct)}{}_{436} = 1 + F^{Y(FRET)}{}_{436}/F^{Y(Direct)}{}_{436}$, and the apparent FRET efficiency (E_{app}) is calculated according to $E_{app} = (\varepsilon_Y/\varepsilon_C) \times (FR - 1)$, where ε_C and ε_Y are molar extinction coefficients of C and Y, respectively. Finally, E_{app} obtained from each cell was plotted against the C/Y ratio as shown in Fig. 4. The true FRET efficiency is the asymptotic value of E_{app} when the C/Y ratio approaches infinity.

Online supplemental material

Fig. S1 shows dose–response curves of the wild-type TMEM16A channel (WT•WT) from 0.1 µM to 10 mM $[Ca^{2+}]$. Fig. S2 shows precisions of E_{rev} measurements are affected by leak current subtraction. Table S1 shows reversal potentials in millivolts (mean ± SEM) for the wild-type TMEM16A channel and various channel constructs harboring the K584Q mutation.

RESULTS

In the absence of Mg^{2+}, the apparent half-effective $[Ca^{2+}]$ ($K_{1/2}$) for activating wild-type TMEM16A chan-

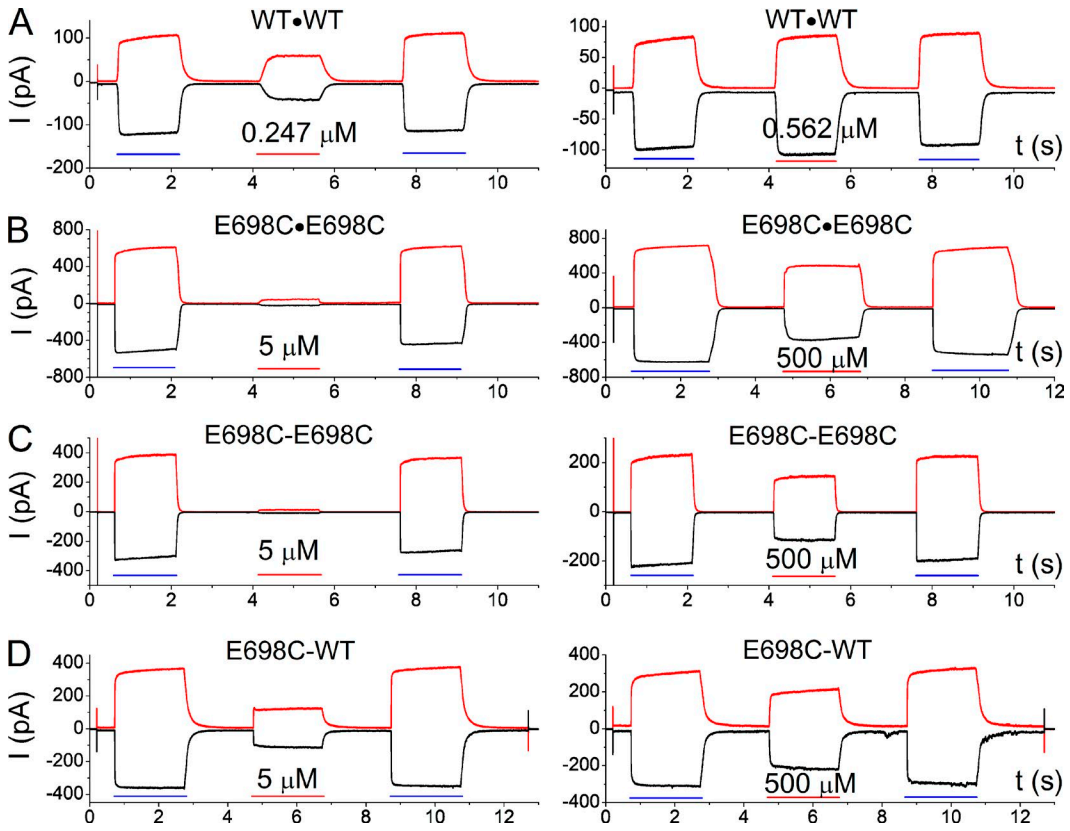

Figure 2. **Recording traces of wild-type TMEM16A and tandemly linked dimers.** Channel currents were induced by a test [Ca^{2+}] pulse (the middle pulse, indicated by red horizontal lines) and two saturating [Ca^{2+}] pulses (indicated by blue horizontal lines) before and after the test pulse for inducing maximal current. Red traces: 40 mV; black traces: −40 mV. (A) Wild-type TMEM16A (namely, WT•WT). (B) E698C•E698C. (C) E698C-E698C. (D) E698C-WT.

nels is in the submicromolar range (Ni et al., 2014). Fig. 2 A illustrates that the WT•WT channel can be significantly activated by 0.247 μM [Ca^{2+}] (Fig. 2 A, left), whereas the current activated by 0.562 μM was close to that activated by 20 μM (Fig. 2 A, right). In comparison, mutations of several acidic residues coordinating Ca^{2+} binding changed the apparent Ca^{2+} affinity by two to three orders of magnitude (Yu et al., 2012; Brunner et al., 2014; Tien et al., 2014), as illustrated in Fig. 2 B, in which 5 μM [Ca^{2+}] activated very little current in E698C•E698C, whereas 500 μM [Ca^{2+}] was not a saturating concentration. These results corroborate the idea that E698 of TMEM16A participates in forming the Ca^{2+}-binding site.

Because TMEM16A is a dimeric channel, the contribution from each subunit activation to the current induction can be evaluated by using a covalently linked tandem dimeric channel in which the mutation that reduces the apparent Ca^{2+} affinity is introduced into one or both subunits. As shown in Fig. 2 C, when two E698C-containing subunits were linked together (namely the E698C-E698C tandem dimer), the Ca^{2+} sensitivity of this concatemer was very similar to that of the channel expressed from the monomeric cDNA construct containing the E698C mutation (namely, E698C•E698C). In contrast, when E698C was introduced to only one subunit (E698C-WT), the heterodimeric mutant channel was significantly activated by 5 μM [Ca^{2+}], whereas 500 μM [Ca^{2+}] was still not a saturating concentration (Fig. 2 D). The heterodimeric mutant channel with a reverse arrangement of the two subunits (namely, WT-E698C) also showed similar results (not depicted).

Comprehensive evaluation of the Ca^{2+} sensitivity in the two subunits was obtained by constructing dose–response curves. The E698C mutants expressed either from the monomeric cDNA construct (E698C•E698C) or from the dimeric cDNA construct (E698C-E698C) exhibited a Ca^{2+}-dependent activation curve easily fit to a single Hill equation, with $K_{1/2}$ in the hundreds of micromolar range. These results are consistent with those reported previously by others (Yu et al., 2012; Brunner et al., 2014; Tien et al., 2014). For the E698C-WT heterodimer, the dose-dependent activation cannot be easily fit by a single Hill equation. Rather, the dose–response activation appeared to occur in two different [Ca^{2+}] ranges, one in the range that activates WT•WT and the other in the range similar to that of activating

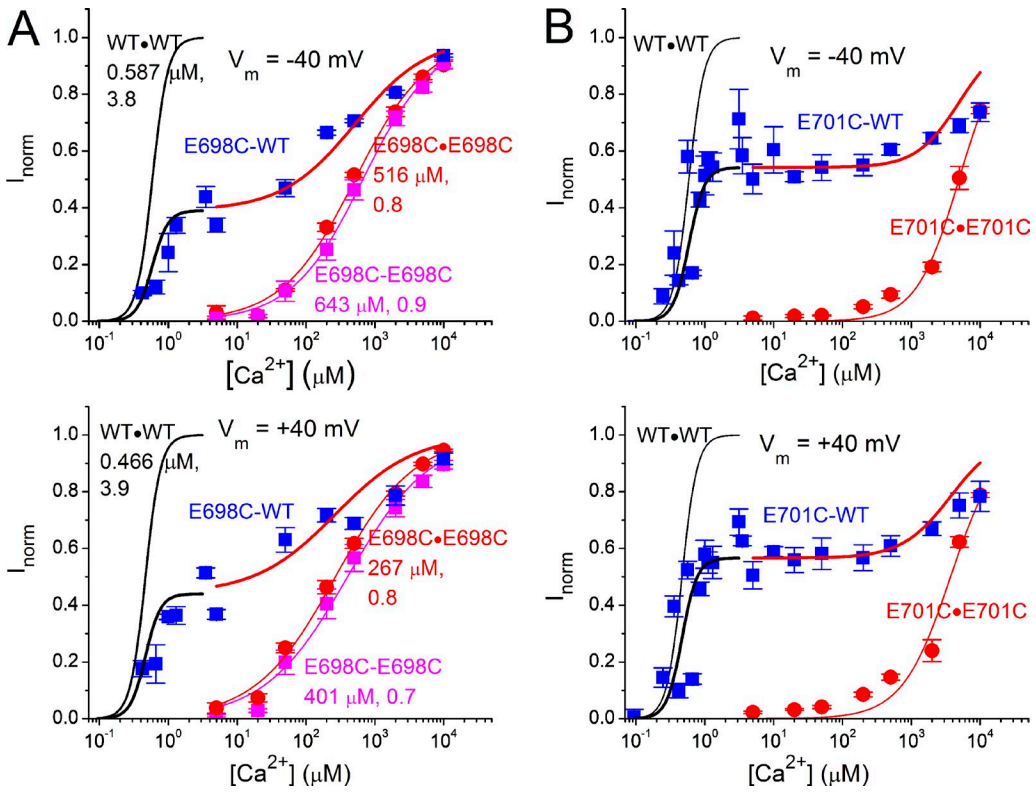

Figure 3. **Dose–response curves of various wild-type and mutant TMEM16A channels.** (A) Comparison of the dose–response curves of WT•WT, E698C•E698C, E698C-E698C, and E698C-WT obtained at −40 mV (top) and 40 mV (bottom). The dose–response curve of the WT•WT channel was obtained from Ni et al. (2014). Values of $K_{1/2}$ (μM) and h for WT•WT, E698C•E698C, and E698C-E698C are shown. The curves for the tandem heterodimeric channel (E698C-WT) in two regions were scaled from the dose–response curves of the WT•WT channel ($I = a \times I_{WT•WT}$, black) and the E698C•E698C channel ($I = a + (1 - a) \times I_{E698C•E698C}$, red), where the values of a (0.39 and 0.44 in the top and bottom panel, respectively) were determined by averaging the values of I_{norm} at $[Ca^{2+}] = 3.13$ μM and $[Ca^{2+}] = 5$ μM. (B) Comparison of the dose–response curves of WT•WT, E701C•E701C, and E701C-WT obtained at −40 mV (top) and 40 mV (bottom). Values of the $K_{1/2}$ and h for E701C•E701C are not depicted because of the lack of current saturation in the dose–response curve. The curves for E701C-WT were scaled from those of the WT•WT channel ($I = b \times I_{WT•WT}$, black) and the E701C•E701C channel ($I = b + (1 - b) \times I_{E701C•E701C}$, red). The values of b (0.542 and 0.566 in the top and bottom panel, respectively) were obtained by averaging the values of I_{norm} at $[Ca^{2+}] = 3.13$ μM and $[Ca^{2+}] = 5$ μM. All data points in A and B are depicted as mean ± SEM. The fitted values of $K_{1/2}$ and Hill coefficient are shown next to the fitted curves.

E698C•E698C or E698C-E698C. Indeed, the dose–response curve resembles a weighted sum of the WT•WT and E698C•E698C dose–response curves (Fig. 3 A). This observation suggests that the two subunits are activated fairly independently; activation of the two subunits can be separated if the two subunits have significantly different Ca^{2+}-binding affinities. To confirm this conclusion, we repeated similar experiments with a different point mutation, E701C (Fig. 3 B), which also altered the apparent Ca^{2+} affinity of the channel (Yu et al., 2012; Brunner et al., 2014; Tien et al., 2014). In fact, the E701C mutation led to an even greater decrease in Ca^{2+} affinity: the decrease in the apparent Ca^{2+} affinity was so drastic that the highest $[Ca^{2+}]$ used in constructing the dose–response curve (10 mM) was not even a saturating concentration as compared with an even higher $[Ca^{2+}]$ (20 mM). Nonetheless, the dose–response relationship obtained from the E701C-WT heterodimer also appears to be a weighted sum of the dose–response curves of the WT•WT channel and the E701C•E701C mutant (Fig. 3 B).

It has been reported that tandem linkage of channel subunits may not ensure the stoichiometry of expressed channels (McCormack et al., 1992). To exclude the possibility that the aforementioned data resulted from two separate populations of WT•WT and E698C•E698C channels because of the assembly of the same subunit (WT or MT) from two E698C-WT heterodimeric molecules, we conducted a FRET analysis with cerulean (C) or eYFP (Y) tagging on the C terminus of the channel protein. FRET is a highly sensitive measurement of distance between the FRET donor (here C) and FRET acceptor (Y; Bykova et al., 2006). Fig. 4 shows that coexpressing WT-C and WT-Y subunits resulted in a positive FRET signal at high C/Y ratios (black symbols), indicating that the C and Y tags from different subunits are close enough to allow for FRET. This result is consistent with a previous FRET study in TMEM16A channels

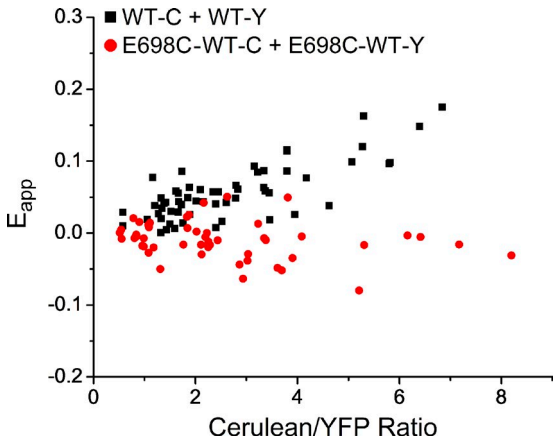

Figure 4. **Comparison of the apparent FRET efficiencies (E_{app}) between C/Y-tagged monomeric WT constructs (black) or C/Y-tagged tandem E698C-WT dimeric constructs (red).**

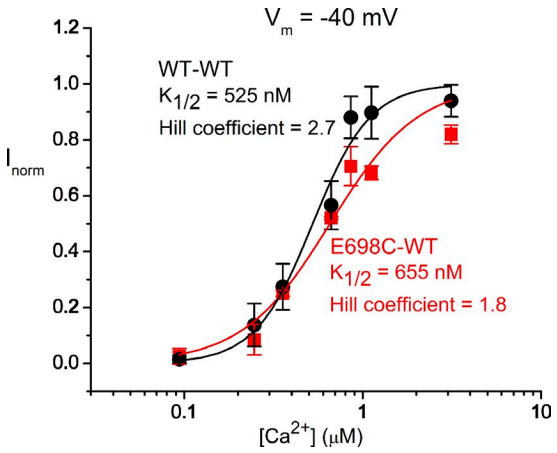

Figure 5. **Dose–response curves of the WT-WT linked homodimer and the E698C-WT linked heterodimer at [Ca^{2+}] < 5 μM.** All current was normalized to that obtained with 5 μM [Ca^{2+}]. Error bars represent SEM. The fitted values of $K_{1/2}$ and Hill coefficient are shown next to the fitted curves.

(Sheridan et al., 2011). In comparison, coexpression of E698C-WT-C and E698C-WT-Y (Fig. 4, red symbols) did not show a detectable FRET signal. These results indicate that the WT subunit in the heterodimer did not assemble with the WT subunit of another heterodimer to form a WT•WT channel, and likewise, the two E698C subunits from two heterodimers do not form an E698C•E698C mutant.

The aforementioned results thus suggest that the current of the E698C-WT channel activated by [Ca^{2+}] < 20 μM is caused by the activation of the high-affinity WT subunit. We thus expect that the dose–response curve of the E698C-WT channel should be similar to that of the WT•WT or the WT-WT channel in low [Ca^{2+}] where activation of the E698C-containing subunit is minimal. Fig. 5 shows a comparison of the dose–response curves of the WT-WT channel and the E698C-WT channel in [Ca^{2+}] < 5 μM. Fitting the data points to the Hill equation gave $K_{1/2}$ = 655 nM and Hill coefficient h = 1.8 for the E698C-WT heterodimer and $K_{1/2}$ = 525 nM and h = 2.7 for the WT-WT channel, indicating that impairing the affinity in one subunit does not drastically affect the other subunit. However, the overall apparent Ca^{2+} sensitivity of the WT subunit of the heterodimer may be slightly diminished compared with that of the WT-WT channel because the heterodimer appears to have a larger $K_{1/2}$ and a smaller Hill coefficient.

The results shown above demonstrate independent activation of the two subunits of the TMEM16A channel. However, whether activation of separate subunits is associated with different pore openings is still not clear. To address this question, we initially planned to generate, in a particular subunit, the K584Q mutation, which was reported to alter the P_{Cl}/P_{Na} permeability ratio of the pore (Yang et al., 2012). Unfortunately, we were unable to observe the change of P_{Cl}/P_{Na} caused by the K584Q mutation (Fig. 6, A and B). The reversal potentials measured in different intracellular [NaCl] (140 mM vs. 84 mM or 140 mM vs. 42 mM) were all similar among various channel constructs whether the K584Q mutation was introduced in only one subunit or in both subunits (Fig. 6 B; also see Table S1). The failure of altering P_{Cl}/P_{Na} by the K584Q mutation excluded our initial plan of using the discrimination of Cl^- versus Na^+ as a pore property to address the pore architecture of TMEM16A.

In constructing I-V relationships, we noticed that with 20 μM [Ca^{2+}] the I-V curve of the K584Q mutant (namely, K584Q mutation in both WT subunit) is outwardly rectified (Fig. 7, A and B). The outward rectification of this mutant is not caused by gating change at different voltages because the I-V relationships obtained from a ramp protocol and from measuring the instantaneous current immediately after step voltage jumps are nearly identical. Furthermore, the rectification of the I-V curve at a much higher [Ca^{2+}] (20 mM) is nearly the same as that obtained in 20 μM (Fig. 7 B). In comparison, the I-V curve of the WT•WT channel is linear (Fig. 7 C, left). Thus, if activation of individual subunits is associated with distinct pores, we expect that the E698C-WT heterodimer containing the K584Q mutant in the E698C subunit, namely, E698C(K584Q)-WT (abbreviated as MT(K584Q)-WT in Fig. 7 C), will have the same I-V curve rectification as the E698C-WT heterodimer when only the WT subunit is activated by low [Ca^{2+}] (such as 20 μM). Experiments in Fig. 7 C (middle) indeed confirmed this prediction. In contrast, when the K584Q mutation was made in the WT subunit of the E698C-WT heterodimer, namely E698C-WT(K584Q) (also abbreviated as MT-WT(K584Q)), the rectification of the I-V curve was significantly more rectified than

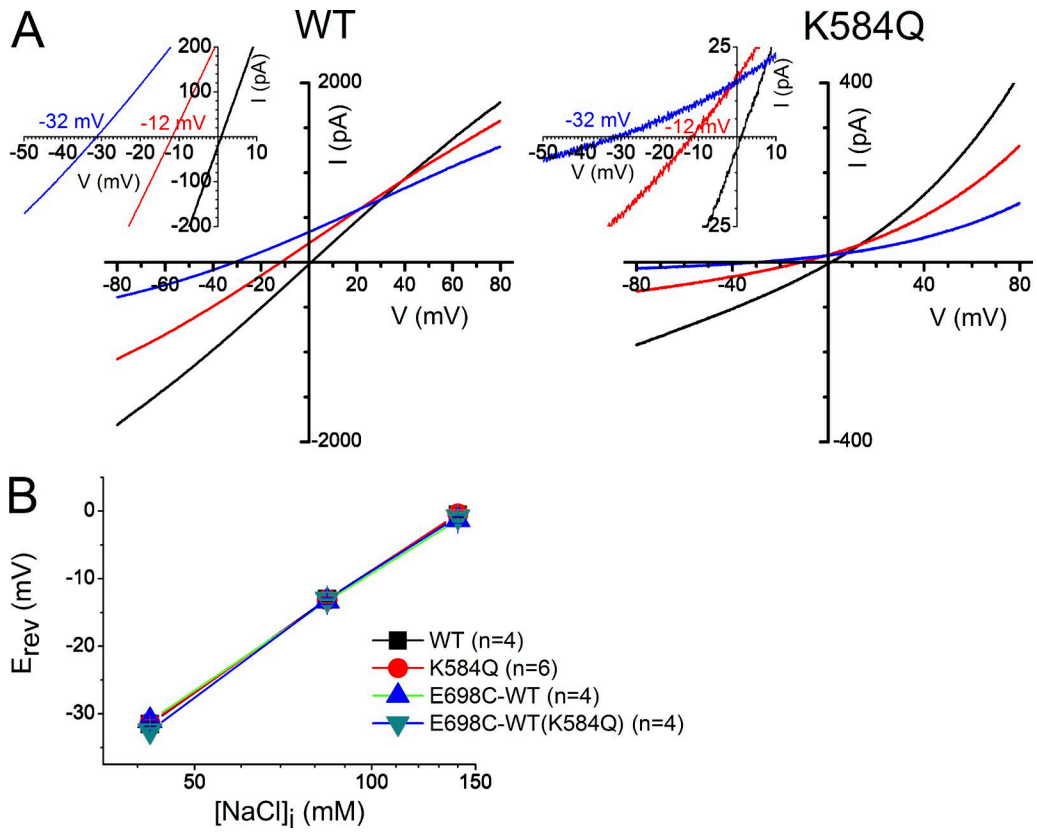

Figure 6. **Comparison of Na^+ and Cl^- permeation properties through the pores of the WT•WT channel (abbreviated as WT) and the K584Q mutant.** (A) I-V curves of the wild-type channel (left) and the K584Q mutant (right) in three $[NaCl]_i$ conditions: 140 mM (black traces), 84 mM (red traces), and 42 mM (blue traces). The reversal potentials (E_{rev}) in each recording are better shown in the inset of each panel. (B) Averaged values of E_{rev} of WT•WT (black), K584Q mutant (red), E698C-WT(K584Q) (green), and E698C(K584Q)-WT (blue) in 140, 84, and 42 mM $[NaCl]_i$. Values of E_{rev} of various channels in the same ionic conditions (Table S1) were not significantly different from one another ($P > 0.05$, one-way ANOVA).

that of the E698C-WT channel (Fig. 7 C, right) and was similar to that of the K584Q mutant.

DISCUSSION

Members of the TMEM16 family are known to consist of two identical subunits (Fallah et al., 2011; Sheridan et al., 2011; Tien et al., 2013; Brunner et al., 2014). The present study examines whether the two subunits of a TMEM16A CaCC can be independently activated by Ca^{2+} and whether activation of different subunits is associated with the opening of different pores. By linking two TMEM16A subunits together, we are able to introduce the mutations that alter the Ca^{2+}-binding affinity to only one subunit. FRET experiments showed that coexpressing E698C-WT-C and E698C-WT-Y did not produce detectable FRET signals between the FRET donor and acceptor (Fig. 4), rendering the possibility less likely that WT•WT and MT•MT channels are formed from assembling two heterodimeric molecules together. Rather, it appears that expressing heterodimeric constructs produces a homogeneous population of channels containing one WT subunit and one MT subunit. Interestingly, the Ca^{2+} dose–response curves in both the E698C-WT and E701C-WT heterodimers can be described by the weighted sum of two Ca^{2+} activation curves, one with a $K_{1/2}$ similar to that of the WT•WT channel in the submicromolar range and the other with a $K_{1/2}$ in the hundreds of micromolar range like that of the mutant channel (Fig. 3).

The biphasic activation by Ca^{2+} can also be observed in wild-type TMEM16A (Fig. S1; also see Lim et al. [2016] for detailed characterization). However, the biphasic activation in the wild-type channel (namely, WT•WT or WT-WT) is very different from that of the heterodimeric channel in several aspects. First, the fractions of the high-affinity versus the low-affinity components of the dose–response curves are different between the wild-type channel and the heterodimer. In the WT•WT channel, the low-affinity component of the dose–response curve (namely, the fraction of the current activated by $[Ca^{2+}] > 20$ µM) is ∼25–30% of that of the total current induced by 20 mM $[Ca^{2+}]$ (Fig. S1). In the heterodimer, the fraction of the low-affinity component is much larger, at least 50%, possibly up to 70%, of the maximal current obtained at $[Ca^{2+}] = 20$ mM (Fig. 3). Second, the $K_{1/2}$ of

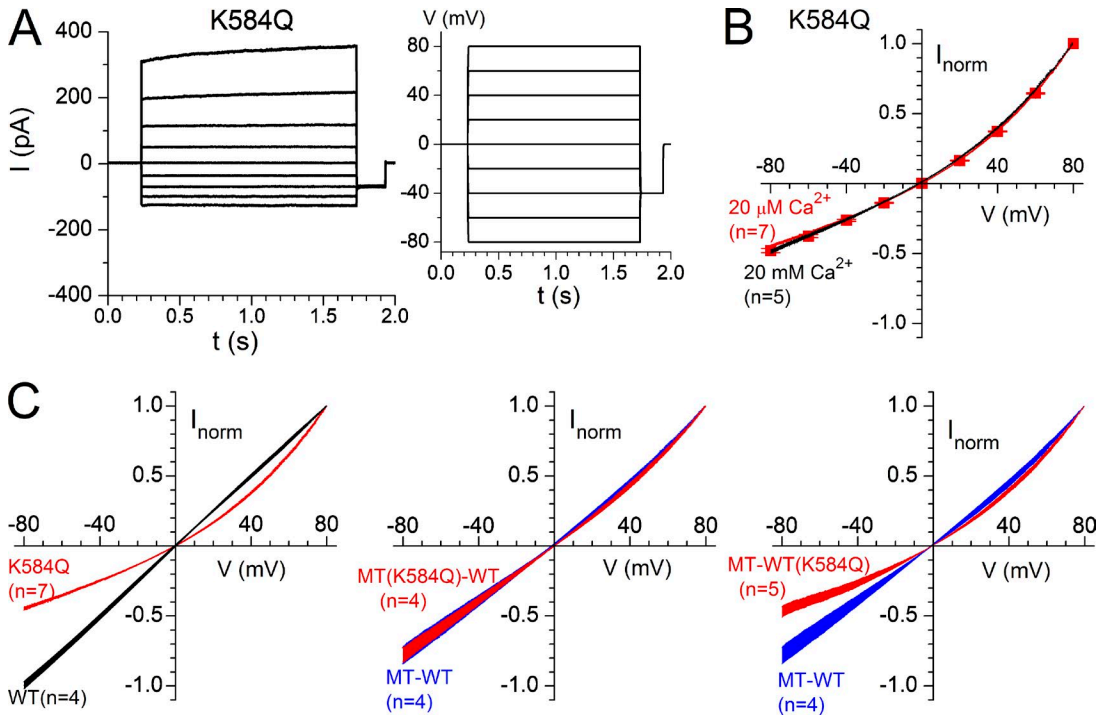

Figure 7. **Pore properties of the wild-type TMEM16A channel, K584Q mutant, and the MT-WT(K584Q) and MT(K584Q)-WT heterodimeric channels, where MT refers to the E698C subunit.** WT(K584Q) and MT(K584Q), respectively, represent the WT and E698C subunits harboring K584Q mutation. $[Cl^-]_i = [Cl^-]_o = 140$ mM in all recordings. (A) Recordings of the K584Q mutant in 20 μM $[Ca^{2+}]$ (left) in response to a voltage step family from −80 to 80 mV (right). Leak current has been subtracted. (B) I-V relationships of the K584Q mutant obtained from a ramp voltage protocol (−80 to 80 mV) in 20 mM $[Ca^{2+}]$ (black) and 20 μM $[Ca^{2+}]$ (red) and from a voltage step protocol like that shown in A (red squares, $n = 5$). For the two ramp I-V curves, the width of each curve represents the SEM of the averaged current of each digitized data point in the I-V curve. RI = 0.45 ± 0.01 ($n = 7$) and 0.48 ± 0.01 ($n = 5$) for the I-V curves in 20 μM $[Ca^{2+}]$ and 20 mM $[Ca^{2+}]$, respectively. (C) Comparison of the I-V curve rectifications between the wild-type channel and K584Q mutant (left) and between E698C-WT (abbreviated as MT-WT; blue) and MT(K584Q)-WT (red, middle) or MT-WT(K584Q) (red, right). All I-V curves were obtained with 20 μM $[Ca^{2+}]$. Four to seven normalized I-V curves were averaged. The width of each I-V curve represents the SEM of the averaged values. RIs for WT, K584Q, MT-WT, MT(K584Q)-WT, and MT-WT(K584Q) were 1.00 ± 0.02, 0.45 ± 0.01, 0.78 ± 0.06, 0.78 ± 0.05, and 0.47 ± 0.04, respectively.

the low-affinity component of the wild-type channel was ~2 mM, whereas in the heterodimer the $K_{1/2}$ appears to depend on the mutation made in the affinity-altered subunit because scaling the dose–response curve of the mutant appears to describe the low-affinity component well (Fig. 3). Finally, the biphasic activation of the wild-type channel can never explain the different Ca^{2+} activation between the mutant homodimer (such as E698C•E698C or E698C-E698C) and the heterodimer (such as E698C-WT). For example, with 5 μM $[Ca^{2+}]$, the current activated in E698C•E698C (or E698C-E698C) is very small (Fig. 2, B and C). However, by replacing one E698C subunit with the WT subunit (the E698C-WT heterodimer), the current activated by the same $[Ca^{2+}]$ is significantly increased (Fig. 2 D). In comparison, 5 μM $[Ca^{2+}]$ already activates at least 70% of the maximal current in the WT•WT channel (Fig. S1). Thus, the most straightforward interpretation for the biphasic dose–response curve of the heterodimer is an independent activation of the two subunits of the heterodimeric channel instead of the biphasic activation of the WT subunit.

The independent activation of the two TMEM16A subunits does not necessarily mean that different subunit activation leads to the opening of distinct pores. It is arguable that only one pore could exist in a channel and that activation of one subunit contributes to a partial opening of the pore. To explore whether the activation of individual subunits is associated with the opening of separate pores, we first attempted to take advantage of the altered discrimination of Cl^- from Na^+ by K584Q mutation and link this mutation to individual subunits. The ion permeation through TMEM16 proteins has been thought not to be particularly selective in discriminating anions from cations. For example, the current associated with the activation of TMEM16F is contributed significantly by Na^+ (Yang et al., 2012; Adomaviciene et al., 2013; Yu et al., 2015a), with a P_{Na}/P_{Cl} ratio estimated to be as high as 6.8 in one previous study (Yang et al., 2012). However, other studies still consider TMEM16F as more anion selective (Grubb et al., 2013; Shimizu et al., 2013), and a P_{Na}/P_{Cl} ratio of ~0.3 had been estimated by Grubb et al. (2013).

Compared with TMEM16F, TMEM16A is much more anion selective, but even so, a P_{Cl}/P_{Na} ratio of only ∼7 was reported (Yang et al., 2012). The mechanism underlying the different selectivity for anions versus cations between TMEM16A and TMEM16F was thought to be caused by a positively charged lysine residue, K584, in TMEM16A versus a corresponding uncharged glutamine residue, Q559, in TMEM16F; mutation of K584 in TMEM16A into a glutamine residue (K584Q) was shown to reduce the P_{Cl}/P_{Na} ratio from 7.0 to 4.1, whereas mutating the corresponding residue from Q to K in TMEM16F (Q559K) reduced the P_{Na}/P_{Cl} of TMEM16F from 6.8 to 2.2 (Yang et al., 2012). These results thus suggested the possibility that K584 residue could be located in the TMEM16A channel pore to discriminate anions from cations.

However, our data shown in Fig. 6 do not support the conclusion that K584 is critical for discriminating Cl^- from Na^+ in the TMEM16A channel pore. In fact, our results showed that the I-V curves of the wild-type channel and the K584Q mutant have indistinguishable reversal potentials in various intracellular [NaCl] (Fig. 6 B). Furthermore, the calculated P_{Cl}/P_{Na} ratio for the wild-type channel from our experiments is much higher than that reported previously. The reversal potentials of the WT•WT channel in our measurements were −31.5 ± 0.3 mV, −13.0 ± 0.4 mV, and −0.5 ± 0.5 mV in 0.3×, 0.6×, and 1× intracellular [NaCl], respectively (Fig. 6 B). For comparison, theoretical values of E_{rev} in 0.3× and 0.6× solutions based on the Goldman-Hodgkin-Katz equation would be −21.8 mV and −9.6 mV, −28.2 mV and −12.1 mV, and −29.8 mV and −12.7 mV when P_{Cl}/P_{Na} ratios are 7, 30, and 100, respectively (T = 295°K). Our results thus suggest that the permeability of Na^+ through the TMEM16A pore is negligible in comparison with the Cl^- permeability. Studies from others have also suggested that TMEM16A has a nearly ideal anionic selectivity (Yang et al., 2008; Terashima et al., 2013). The reasons for the qualitative and quantitative differences between our results and those reported in Yang et al. (2012) are not clear to us, but we suspect that differences in experimental methods, for example, using NMDG-SO_4 versus sucrose to replace intracellular NaCl (Lim et al., 2016), and/or analyses (such as subtraction of the endogenous leak current; Fig. S2) may explain the discrepancy.

Although we are unable to confirm that residue K584 helps in discriminating anions versus cations for TMEM16A, our experiments do suggest that K584 is a pore residue because of the prominent rectification of the I-V curve of the K584Q mutant in symmetrical 140 mM [NaCl]. The I-V curve of the wild-type TMEM16A pore in a saturating $[Ca^{2+}]$ is linear with a unity RI. In contrast, the I-V curve of the K584Q mutant is outwardly rectified (RI = ∼0.45; Fig. 7). This outward rectification in K584Q is not caused by the voltage-dependent change of gating properties because the same rectification is observed in the I-V relationship constructed from instantaneous currents upon jumping membrane potential to various voltages (Fig. 7 B). Furthermore, with 20 mM $[Ca^{2+}]$, the I-V curve of the K584Q mutant remains outwardly rectified (Fig. 7 B). It is possible that K584 is located at the intracellular pore entrance, and therefore the positive charge on the sidechain helps recruit Cl^- to the intracellular pore entrance, similar to the electrostatic control of the conductance of CLC-0 by a lysine residue (Middleton et al., 1996; Chen and Chen, 2003).

If there are separate pores associated with different subunits and if the I-V curve rectification caused by the K584Q mutation is indeed a pore property, we expect that introducing K584Q mutation to the WT subunit or to the E698C-containing subunit in the E698C-WT heterodimer would produce different degrees of I-V curve rectification when only the high-affinity WT subunit is activated. Fig. 7 C indeed shows the fulfillment of this prediction, indicating that activation of different subunits is associated with the opening of distinct pores. Thus, it appears that the TMEM16A channel may also contain multiple (most likely two) pores, and Ca^{2+} activation of an individual subunit opens the pore associated with that activated subunit. This scenario is similar to the "double-barrel" feature of CLC channels (Miller, 1982; Miller and White, 1984; Ludewig et al., 1996; Middleton et al., 1996), except that the opening of the CLC channel pores is apparently voltage dependent, whereas the TMEM16A pores are opened by ligand binding.

Although the results presented in this study suggest that activation of different subunits of TMEM16A opens distinct pores, the exact mechanism of TMEM16A activation is still a subject of much speculation. The fact that the wild-type TMEM16A channel has a dose–response curve with a Hill coefficient $h > 1$ indicates cooperative binding of multiple Ca^{2+} in the channel activation process. Our observation that the dose–response curve of the E698C-WT channel in the range of $[Ca^{2+}] < 5$ µM still has a Hill coefficient substantially greater than 1 (Fig. 5) indicates multiple Ca^{2+}-binding sites within one subunit, consistent with the high-resolution crystal structure of the nhTMEM16 molecule. Nonetheless, it appears that the cooperativity of channel opening may not all come from Ca^{2+} binding within one subunit because the dose–response curve of the E698C-WT in the low $[Ca^{2+}]$ range (<5 µM) has a lower apparent affinity and a smaller Hill coefficient than that of the WT-WT channel. This observation suggests that some cooperativity in the channel activation resulting from cross-talk of the two subunits cannot be ruled out. Finally, the activation of the wild-type channel by $[Ca^{2+}]$ in the mM range (Fig. S1) may suggest low-affinity Ca^{2+}-binding sites not seen in the nhTMEM16 crystal structure.

In conclusion, by constructing covalent tandem dimers for TMEM16A channels and introducing muta-

tions to specific subunits, we altered the Ca^{2+}-binding affinity and induced the rectification of the channel current associated with individual subunits. Our results suggest that the two subunits with different apparent Ca^{2+} affinities can be independently activated and that the activation of individual subunits is associated with the opening of separate pores. Thus, the pore architecture of TMEM16A appears to be similar to the "double-barrel" structure found in members of the CLC channel/transporter family.

ACKNOWLEDGMENTS

We thank Mr. Dung Nguyen for technical assistance in this project. We also thank Drs. Robert Fairclough, Takashi Kurahashi, and Hiroko Takeuchi for helpful discussion and critical reading of the manuscript.

This work was partially supported by National Institutes of Health grant R01GM065447 and by the Jong L. Chen Family Neuroscience Research Fund.

The authors declare no competing financial interests.

Merritt Maduke served as editor.

Submitted: 21 June 2016
Accepted: 30 September 2016

REFERENCES

Adomaviciene, A., K.J. Smith, H. Garnett, and P. Tammaro. 2013. Putative pore-loops of TMEM16/anoctamin channels affect channel density in cell membranes. *J. Physiol.* 591:3487–3505. http://dx.doi.org/10.1113/jphysiol.2013.251660

Bevers, E.M., and P.L. Williamson. 2016. Getting to the outer leaflet: Physiology of phosphatidylserine exposure at the plasma membrane. *Physiol. Rev.* 96:605–645. http://dx.doi.org/10.1152/physrev.00020.2015

Bolduc, V., G. Marlow, K.M. Boycott, K. Saleki, H. Inoue, J. Kroon, M. Itakura, Y. Robitaille, L. Parent, F. Baas, et al. 2010. Recessive mutations in the putative calcium-activated chloride channel Anoctamin 5 cause proximal LGMD2L and distal MMD3 muscular dystrophies. *Am. J. Hum. Genet.* 86:213–221. http://dx.doi.org/10.1016/j.ajhg.2009.12.013

Brunner, J.D., N.K. Lim, S. Schenck, A. Duerst, and R. Dutzler. 2014. X-ray structure of a calcium-activated TMEM16 lipid scramblase. *Nature.* 516:207–212. http://dx.doi.org/10.1038/nature13984

Bykova, E.A., X.D. Zhang, T.Y. Chen, and J. Zheng. 2006. Large movement in the C terminus of CLC-0 chloride channel during slow gating. *Nat. Struct. Mol. Biol.* 13:1115–1119. http://dx.doi.org/10.1038/nsmb1176

Caputo, A., E. Caci, L. Ferrera, N. Pedemonte, C. Barsanti, E. Sondo, U. Pfeffer, R. Ravazzolo, O. Zegarra-Moran, and L.J. Galietta. 2008. TMEM16A, a membrane protein associated with calcium-dependent chloride channel activity. *Science.* 322:590–594. http://dx.doi.org/10.1126/science.1163518

Chen, M.F., and T.Y. Chen. 2003. Side-chain charge effects and conductance determinants in the pore of ClC-0 chloride channels. *J. Gen. Physiol.* 122:133–145. http://dx.doi.org/10.1085/jgp.200308844

Dutzler, R., E.B. Campbell, M. Cadene, B.T. Chait, and R. MacKinnon. 2002. X-ray structure of a ClC chloride channel at 3.0 A reveals the molecular basis of anion selectivity. *Nature.* 415:287–294. http://dx.doi.org/10.1038/415287a

Dutzler, R., E.B. Campbell, and R. MacKinnon. 2003. Gating the selectivity filter in ClC chloride channels. *Science.* 300:108–112. http://dx.doi.org/10.1126/science.1082708

Fallah, G., T. Römer, S. Detro-Dassen, U. Braam, F. Markwardt, and G. Schmalzing. 2011. TMEM16A(a)/anoctamin-1 shares a homodimeric architecture with CLC chloride channels. *Mol. Cell. Proteomics.* 10:M110.004697. http://dx.doi.org/10.1074/mcp.M110.004697

Ferrera, L., A. Caputo, I. Ubby, E. Bussani, O. Zegarra-Moran, R. Ravazzolo, F. Pagani, and L.J. Galietta. 2009. Regulation of TMEM16A chloride channel properties by alternative splicing. *J. Biol. Chem.* 284:33360–33368. http://dx.doi.org/10.1074/jbc.M109.046607

Grubb, S., K.A. Poulsen, C.A. Juul, T. Kyed, T.K. Klausen, E.H. Larsen, and E.K. Hoffmann. 2013. TMEM16F (Anoctamin 6), an anion channel of delayed Ca^{2+} activation. *J. Gen. Physiol.* 141:585–600. http://dx.doi.org/10.1085/jgp.201210861

Hartzell, C., I. Putzier, and J. Arreola. 2005. Calcium-activated chloride channels. *Annu. Rev. Physiol.* 67:719–758. http://dx.doi.org/10.1146/annurev.physiol.67.032003.154341

Hicks, D., A. Sarkozy, N. Muelas, K. Koehler, A. Huebner, G. Hudson, P.F. Chinnery, R. Barresi, M. Eagle, T. Polvikoski, et al. 2011. A founder mutation in Anoctamin 5 is a major cause of limb-girdle muscular dystrophy. *Brain.* 134:171–182. http://dx.doi.org/10.1093/brain/awq294

Huang, F., X. Wong, and L.Y. Jan. 2012. International Union of Basic and Clinical Pharmacology. LXXXV: Calcium-activated chloride channels. *Pharmacol. Rev.* 64:1–15. http://dx.doi.org/10.1124/pr.111.005009

Katoh, M., and M. Katoh. 2004. GDD1 is identical to TMEM16E, a member of the TMEM16 family. *Am. J. Hum. Genet.* 75:927–928. http://dx.doi.org/10.1086/425341

Kunzelmann, K., B. Nilius, G. Owsianik, R. Schreiber, J. Ousingsawat, L. Sirianant, P. Wanitchakool, E.M. Bevers, and J.W. Heemskerk. 2014. Molecular functions of anoctamin 6 (TMEM16F): a chloride channel, cation channel, or phospholipid scramblase? *Pflugers Arch.* 466:407–414. http://dx.doi.org/10.1007/s00424-013-1305-1

Lhermusier, T., H. Chap, and B. Payrastre. 2011. Platelet membrane phospholipid asymmetry: from the characterization of a scramblase activity to the identification of an essential protein mutated in Scott syndrome. *J. Thromb. Haemost.* 9:1883–1891. http://dx.doi.org/10.1111/j.1538-7836.2011.04478.x

Lim, N.K., A.K.M. Lam, and R. Dutzler. 2016. Independent activation of ion conduction pores in the double-barreled calcium-activated chloride channel TMEM16A. *J. Gen. Physiol.* http://dx.doi.org/10.1085/jgp.201611650

Ludewig, U., M. Pusch, and T.J. Jentsch. 1996. Two physically distinct pores in the dimeric ClC-0 chloride channel. *Nature.* 383:340–343. http://dx.doi.org/10.1038/383340a0

Mahjneh, I., J. Jaiswal, A. Lamminen, M. Somer, G. Marlow, S. Kiuru-Enari, and R. Bashir. 2010. A new distal myopathy with mutation in anoctamin 5. *Neuromuscul. Disord.* 20:791–795. http://dx.doi.org/10.1016/j.nmd.2010.07.270

Malvezzi, M., M. Chalat, R. Janjusevic, A. Picollo, H. Terashima, A.K. Menon, and A. Accardi. 2013. Ca^{2+}-dependent phospholipid scrambling by a reconstituted TMEM16 ion channel. *Nat. Commun.* 4:2367. http://dx.doi.org/10.1038/ncomms3367

Marconi, C., P. Brunamonti Binello, G. Badiali, E. Caci, R. Cusano, J. Garibaldi, T. Pippucci, A. Merlini, C. Marchetti, K.J. Rhoden, et al. 2013. A novel missense mutation in ANO5/TMEM16E is causative for gnathodiaphyseal dyplasia in a large Italian pedigree. *Eur. J. Hum. Genet.* 21:613–619. http://dx.doi.org/10.1038/ejhg.2012.224

McCormack, K., L. Lin, L.E. Iverson, M.A. Tanouye, and F.J. Sigworth. 1992. Tandem linkage of Shaker K+ channel subunits does not ensure the stoichiometry of expressed channels.

Biophys. J. 63:1406–1411. http://dx.doi.org/10.1016/S0006-3495(92)81703-4

Middleton, R.E., D.J. Pheasant, and C. Miller. 1996. Homodimeric architecture of a ClC-type chloride ion channel. *Nature.* 383:337–340. http://dx.doi.org/10.1038/383337a0

Miller, C. 1982. Open-state substructure of single chloride channels from Torpedo electroplax. *Philos. Trans. R. Soc. Lond. B Biol. Sci.* 299:401–411. http://dx.doi.org/10.1098/rstb.1982.0140

Miller, C., and M.M. White. 1984. Dimeric structure of single chloride channels from Torpedo electroplax. *Proc. Natl. Acad. Sci. USA.* 81:2772–2775. http://dx.doi.org/10.1073/pnas.81.9.2772

Ni, Y.L., A.S. Kuan, and T.Y. Chen. 2014. Activation and inhibition of TMEM16A calcium-activated chloride channels. *PLoS One.* 9:e86734. http://dx.doi.org/10.1371/journal.pone.0086734

Pedemonte, N., and L.J. Galietta. 2014. Structure and function of TMEM16 proteins (anoctamins). *Physiol. Rev.* 94:419–459. http://dx.doi.org/10.1152/physrev.00039.2011

Picollo, A., M. Malvezzi, and A. Accardi. 2015. TMEM16 proteins: unknown structure and confusing functions. *J. Mol. Biol.* 427:94–105. http://dx.doi.org/10.1016/j.jmb.2014.09.028

Schroeder, B.C., T. Cheng, Y.N. Jan, and L.Y. Jan. 2008. Expression cloning of TMEM16A as a calcium-activated chloride channel subunit. *Cell.* 134:1019–1029. http://dx.doi.org/10.1016/j.cell.2008.09.003

Scudieri, P., E. Sondo, L. Ferrera, and L.J. Galietta. 2012. The anoctamin family: TMEM16A and TMEM16B as calcium-activated chloride channels. *Exp. Physiol.* 97:177–183. http://dx.doi.org/10.1113/expphysiol.2011.058198

Sheridan, J.T., E.N. Worthington, K. Yu, S.E. Gabriel, H.C. Hartzell, and R. Tarran. 2011. Characterization of the oligomeric structure of the Ca^{2+}-activated Cl^- channel Ano1/TMEM16A. *J. Biol. Chem.* 286:1381–1388. http://dx.doi.org/10.1074/jbc.M110.174847

Shimizu, T., T. Iehara, K. Sato, T. Fujii, H. Sakai, and Y. Okada. 2013. TMEM16F is a component of a Ca^{2+}-activated Cl^- channel but not a volume-sensitive outwardly rectifying Cl^- channel. *Am. J. Physiol. Cell Physiol.* 304:C748–C759. http://dx.doi.org/10.1152/ajpcell.00228.2012

Suzuki, J., M. Umeda, P.J. Sims, and S. Nagata. 2010. Calcium-dependent phospholipid scrambling by TMEM16F. *Nature.* 468:834–838. http://dx.doi.org/10.1038/nature09583

Suzuki, J., T. Fujii, T. Imao, K. Ishihara, H. Kuba, and S. Nagata. 2013. Calcium-dependent phospholipid scramblase activity of TMEM16 protein family members. *J. Biol. Chem.* 288:13305–13316. http://dx.doi.org/10.1074/jbc.M113.457937

Terashima, H., A. Picollo, and A. Accardi. 2013. Purified TMEM16A is sufficient to form Ca^{2+}-activated Cl^- channels. *Proc. Natl. Acad. Sci. USA.* 110:19354–19359. http://dx.doi.org/10.1073/pnas.1312014110

Tien, J., H.Y. Lee, D.L. Minor Jr., Y.N. Jan, and L.Y. Jan. 2013. Identification of a dimerization domain in the TMEM16A calcium-activated chloride channel (CaCC). *Proc. Natl. Acad. Sci. USA.* 110:6352–6357. (published erratum appears in *Proc. Natl. Acad. USA.* 2016. 113:E5775) http://dx.doi.org/10.1073/pnas.1303672110

Tien, J., C.J. Peters, X.M. Wong, T. Cheng, Y.N. Jan, L.Y. Jan, and H. Yang. 2014. A comprehensive search for calcium binding sites critical for TMEM16A calcium-activated chloride channel activity. *eLife.* 3:e02772. http://dx.doi.org/10.7554/eLife.02772

Tsutsumi, S., N. Kamata, T.J. Vokes, Y. Maruoka, K. Nakakuki, S. Enomoto, K. Omura, T. Amagasa, M. Nagayama, F. Saito-Ohara, et al. 2004. The novel gene encoding a putative transmembrane protein is mutated in gnathodiaphyseal dysplasia (GDD). *Am. J. Hum. Genet.* 74:1255–1261. http://dx.doi.org/10.1086/421527

Yang, H., A. Kim, T. David, D. Palmer, T. Jin, J. Tien, F. Huang, T. Cheng, S.R. Coughlin, Y.N. Jan, and L.Y. Jan. 2012. TMEM16F forms a Ca^{2+}-activated cation channel required for lipid scrambling in platelets during blood coagulation. *Cell.* 151:111–122. http://dx.doi.org/10.1016/j.cell.2012.07.036

Yang, Y.D., H. Cho, J.Y. Koo, M.H. Tak, Y. Cho, W.S. Shim, S.P. Park, J. Lee, B. Lee, B.M. Kim, et al. 2008. TMEM16A confers receptor-activated calcium-dependent chloride conductance. *Nature.* 455:1210–1215. http://dx.doi.org/10.1038/nature07313

Yu, K., C. Duran, Z. Qu, Y.Y. Cui, and H.C. Hartzell. 2012. Explaining calcium-dependent gating of anoctamin-1 chloride channels requires a revised topology. *Circ. Res.* 110:990–999. http://dx.doi.org/10.1161/CIRCRESAHA.112.264440

Yu, K., J.M. Whitlock, K. Lee, E.A. Ortlund, Y.Y. Cui, and H.C. Hartzell. 2015a. Identification of a lipid scrambling domain in ANO6/TMEM16F. *eLife.* 4:e06901. http://dx.doi.org/10.7554/eLife.06901

Yu, Y., A.S. Kuan, and T.Y. Chen. 2014. Calcium-calmodulin does not alter the anion permeability of the mouse TMEM16A calcium-activated chloride channel. *J. Gen. Physiol.* 144:115–124. http://dx.doi.org/10.1085/jgp.201411179

Yu, Y., M.F. Tsai, W.P. Yu, and T.Y. Chen. 2015b. Modulation of the slow/common gating of CLC channels by intracellular cadmium. *J. Gen. Physiol.* 146:495–508. http://dx.doi.org/10.1085/jgp.201511413